Particle & Particle Systems Characterization
www.particle-journal.com

Controllable Preparation of Hierarchical ZnO Nanocages and its Oxygen Vacancy through the Nanoscale Kirkendall Process

Haosen Fan, Jiaxin Zheng, Jiangtao Hu, Yantao Su, Ning Zhao, Jian Xu, Fusheng Liu, and Feng Pan**

The synthesis of ZnO with tailorable shapes and point defects is important for its potential applications. Here, a facile approach is demonstrated to prepare ZnO nanocages with controllable porous shell structures though sintering a Zn-based cyanide-bridged coordination polymer under different temperatures. The transformation of ZnCP microspheres into ZnO nanocages is based on two types of nanoscale Kirkendall effect, which are related to low temperature solid–solid interfacial oxidation and high temperature solid–gas interfacial reaction, respectively. At low temperature (around 300 °C) and before the ZnCP decomposition, the novel "hierarchical ZnO bigger nanocages embedded with smaller nanocages with 10 nm nanocrystals" can be generated. By contrast, when coming to the total decomposition of ZnCP at 800 °C, ZnO nanocages with significantly increased sizes and large cavities are generated, and large amounts of oxygen vacancies (V_O) are created at the same time, leading to the dramatic increased luminescence intensities of the UV peak due to V_O at 540 nm. Thus, the luminescence intensities versus defect concentration in the prepared ZnO nanocages can also be controlled by tuning the sintering temperatures.

1. Introduction

Zinc oxide, as an important transition metal oxide, is an advanced semiconductor material with a direct band gap (3.37 eV) and a relatively high excitation binding energy (60 meV).[1] Recently, ZnO micro/nanostructures of different dimensions have attracted great interest because of their potential applications in optoelectronic devices,[2] photocatalysis,[3] sensor,[4] drug delivery,[5] and dye-sensitized solar cells.[6] Great attentions have been focused on the synthesis of novel ZnO with hierarchical architectures, and specifically with controllable and tailorable shapes owing to its diverse shape-induced functions. For example, compared with ZnO nanorod-based light-emitting diodes (LEDs), ZnO nanotube-based LEDs were found to have approximately twice the electroluminescence (EL) intensity.[7] ZnO with hollow structures is particularly attractive to be used as the photoanodes for dye-sensitized solar cells due to the high specific surface area for dye molecules absorption, relatively large size for scattering incident light, high electron mobility, and low production cost.[8] Apart from the shape-induced functions, the properties of ZnO are highly sensitive to the nature and concentrations of lattice imperfections,[9] and controllable point defects in ZnO are also very important for its applications and become an extensively studied topic.

Benefited from their advantages of low density, uniform size, and large specific surface area, monodispersed micro/nanohollow structures have attracted considerable interests in the past few decades owing to their potential applications in many fields, such as hydrogen production and storage,[10] energy storage (supercapacitors or rechargeable batteries),[11] and drug release.[12] The strategies for preparing micro/nanohollow structures involve the use of various removable templates, including hard templates (e.g., monodispersed silica, polymer spheres, carbon particles) and soft templates (e.g., micelles, droplets, and gas bubbles).[13] Template-free methods have also been developed for generating hollow micro/nanostructures based on some self-assembly or novel mechanisms, such as the Kirkendall effect,[14] inside–out Ostwald ripening,[15] quasitemplating,[16] and corrosion-based inside–out evacuation.[17]

Recently, coordination polymers (CPs), also called as metal-organic frameworks (MOFs) or porous coordination polymers (PCPs), have aroused great interests in the preparation of hollow structures of metal oxides because of their well-defined

Dr. H. Fan, Dr. J. Zheng, J. Hu, Dr. Y. Su, Prof. F. Pan
School of Advanced Materials
Peking University Shenzhen Graduate School
Shenzhen 518055, P.R. China
E-mail: panfeng@pkusz.edu.cn
Prof. N. Zhao, Prof. J. Xu
Beijing National Laboratory for Molecular Sciences, Laboratory of Polymer Physics and Chemistry
Institute of Chemistry
Chinese Academy of Sciences
Beijing 100190, P.R. China
E-mail: jxu@iccas.ac.cn
Prof. F. Liu
College of Materials Science and Engineering
Shenzhen University and Shenzhen Key Laboratory of Special Functional Materials
Shenzhen 518060, P.R. China

DOI: 10.1002/ppsc.201500011

morphology, high surface areas, adjustable framework compositions, and uniform micropore structures.[18] Among them, prussian blue and its analogues consisting of metal ions (Fe^{3+}, Fe^{2+}, Co^{3+}, or Ni^{2+}) coordinated to rigid organic molecules (cyano groups) have been developed to design and prepare various porous micro/nanostructures from zero- to three-dimension due to their unique size- and shape-dependent properties.[19] For example, Lou and co-workers prepared Fe_2O_3 microboxes with hierarchical shell structures from prussian blue.[20] Yamauchi and co-workers developed a facile way to fabricate highly crystalline prussian blue hollow particles with uniform sizes via a controlled self-etching reaction on prussian blue mesocrystals.[21] Yan et al. reported a novel facile strategy for the fabrication of prussian blue analogue $Co_3[Co(CN)_6]_2$ nanocubes and then obtained Co_3O_4 porous structures based on the Kirkendall effect.[22] Hu et al. demonstrated a new synthetic concept to prepare microporous CPs with multiple nanoarchitectures by etching precursors with a heterogeneous distribution of defects.[23] Those pioneering attempts have explored new ideas for fabricating novel nano/microporous structures and help to get a deep understanding of the relationship of structures, properties, and potential applications of microporous CPs.[24]

Herein, we demonstrate a bottom–up approach to controllable preparation of hierarchical monodispersed ZnO nanocages with porous shell structures based on sintering of a Zn-based cyanide-bridged coordination polymers (prussian blue analogue) of $Zn[Zn(CN)_4]\cdot xH_2O$ microspheres (named as ZnCP) under different temperatures. The ZnO nanocages with different sizes and hollows at the various sintering process were found to be caused from the nanoscale Kirkendall effect, which are related to low temperature solid–solid interfacial oxidation and high temperature solid–gas interfacial reaction before and after the ZnCP decomposition, respectively. We also found that the luminescence versus defect concentration in the prepared ZnO nanocages could be controlled by tuning the sintering temperatures, and the mechanism behind this is discussed in detail.

2. Results and Discussion

As our precursor for preparing ZnO nanocages, ZnCP microspheres is an analogue prussian blue in which the Zn atoms are bridged by neighboring four cyano groups. ZnCP microspheres were simply obtained by adding $K_2[Zn(CN)_4]$ aqueous solution drop wisely into aqueous solution containing $ZnCl_2\cdot 6H_2O$ and polyvinylpyrrolidone (PVP). The resultant ZnCP microspheres can be well dispersed in water to form a colloidal suspension with an obvious Tyndall phenomenon (**Figure 1**a), indicating that the sizes of ZnCP nanocrystals were much less than the wavelength of the incident laser (about 530 nm). Scanning electron microscope (SEM) images (Figure 1b-1 and Supporting Information, Figure S1a) show the synthesized ZnCP microspheres are very uniform with an average diameter of about 1 μm. The polydispersity index of the microspheres determined by light scattering is as low as 1.01 (Supporting Information, Figure S1b). From the high resolution SEM image (Figure 1b-2), lichee-like topography is observed on the surface of the microspheres. Meanwhile, cross-section image of a broken ZnCP microsphere reveals that the microsphere is build up by the aggregation of ZnCP nanoparticles (Figure 1b-3). Transmission electron microscope (TEM) image of a single ZnCP microsphere (Figure 1b-4) clearly exhibits its spherical shape, bumpy profile, and dense nature. The high-resolution TEM image of the edge of the microsphere (Figure 1b-5) demonstrates a good crystallinity, with all the lattice fringes oriented in the same direction. Element mapping analysis is used to confirm the elemental composition of ZnCP microspheres. As shown in Figure 1c, ZnCP microspheres are composed of Zn, C, N, and O elements, which are well-distributed throughout the microsphere, implying a homogeneous construction of the microsphere by the ZnCP nanoparticles. The crystallographic structure and phase purity of the ZnCP microspheres were examined by powder X-ray diffraction (XRD). The diffraction peaks can be unambiguously assigned to body center cubic (bcc) $Zn(CN)_2$ (JCPDS card no. 06–0175; space group *P*-43*m*, a = b = c = 5.905 Å, $\alpha = \beta = \gamma = 90°$) (Supporting Information, Figure S2). No additional diffraction peaks from impurities were detected, indicating a high purity of the product. Hence, ZnCP is composed of two interconnected $Zn(CN)_2$ molecules, and each Zn atom is surrounded by four neighboring cyano groups arranged in a manner of a Zn-centered tetrahedron (Supporting Information, Figure S3).[25] The unit cell of ZnCP is formed by a pair of interpenetrating diamonded networks via linear Zn–CN–Zn linkages of two tetrahedral Zn^{2+} cations.

The obtained ZnCP microspheres can be transformed into ZnO nanocages by thermal oxidation in air. The formation mechanism is schematically depicted in **Figure 2**a. In the initial stage, $Zn(CN)_4^{2-}$ will combine with Zn^{2+} to form $Zn[Zn(CN)_4]$ complex in the reactive system. Then PVP are coordinated to the complex to form nanoscaled complex-PVP micellar coordination particles. In the further growth stage, for minimization of the total energy of the system, the small primary nanoparticles aggregated together to form uniform microspheres.[26] The calcination of the ZnCP microspheres in ambient atmosphere will lead to the oxidative decomposition of cyano groups and formation of ZnO nanocrystals. Thus ZnO nanocages are obtained as shown in Figure 2b, which is produced by thermal oxidation in air at 700 °C. The XRD patterns of the prepared ZnO nanocages (Supporting Information, Figure S4) are in good agreement with the standard values for hexagonal close-packed (hcp) ZnO (JCPDS card no. 36–1451; space group *P*63*mc*, a = 3.25 Å, b = 3.25 Å, c = 5.207 Å, $\alpha = \beta = 90°$, $\gamma = 120°$). The sharp peaks and no additional diffraction indicate the high purity and good crystallinity of the as-prepared sample. As shown in Figure 2b-1, the resultant ZnO nanocages are uniform with a diameter of about 500 nm, smaller than the original ZnCP microspheres owing to the decomposition during the calcination, and they are constructed by the aggregation of ZnO nanocrystals from few tens to a hundred nanometers (Figure 2b-2). Holes can be observed on the surface. Moreover, the cracked ZnO nanocages further are proved to be indeed hollow (Figure 2b-3). TEM image of a single nanocage further clearly demonstrates its cage-like structure and porous shell stacked randomly by ZnO nanocrystals. The selected area electron diffraction (SAED) pattern (inset of Figure 2b-4) exhibits multiple ring-like diffraction modes, indicating the polycrystalline nature of the as-formed ZnO. The rings are assigned to diffraction from (1 0 0), (1 0 1), (1 1 0),

DOI: 10.1002/ppsc.201500011

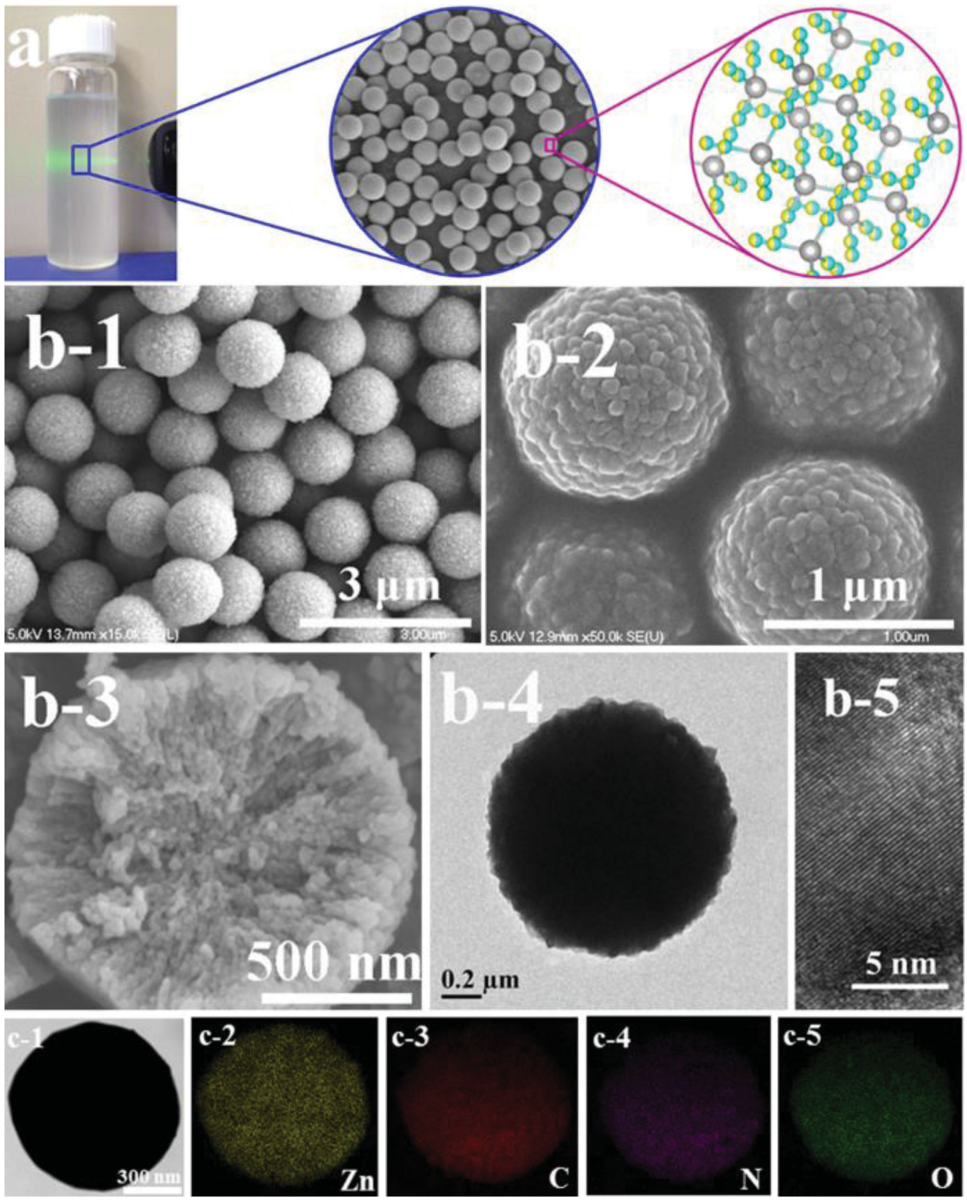

Figure 1. a) Photographs of colloidal suspensions containing well dispersed ZnCP microspheres with obvious Tyndall effect. b1–b5) SEM and TEM images of as-prepared monodispersed ZnCP microspheres. c) HAADF-STEM and elemental mapping of ZnCP microspheres.

and (1 0 3) planes. The high-resolution TEM image of the edge part of the ZnO nanocrystal shows the obvious lattice fringes mainly oriented in three directions, demonstrating the lattice spacing of 0.25, 0.26, and 0.28 nm, which corresponds to the distance between (1011), (0002), and (1010) planes (Figure 2b-5,b-6), respectively. In addition, energy dispersive spectroscopy (EDS) mapping was used to evaluate the composition and distribution uniformity of the Zn and the O elements within the nanocages. As shown in Figure 2c, it is clear that the nanocages are indeed composed of Zn and O elements, which distribute uniformly in a single nanocage. Besides, the mixed elements mapping image further presents a homogenous distribution of zinc and oxygen to form an entire nanocage (Figure 2c-4).

In order to further understand the transformation mechanism from ZnCP microspheres to ZnO nanocages and related structures and properties, the ZnCP microspheres were calcinated at several different temperature zones according to thermogravimetry (TG), which can be divided as three temperature zones, such as (1) around 300 °C (zone-1), (2) 300—700 °C (zone-2), and (3) around 800 °C (zone-3) (shown in Supporting Information, Figure S6). When the sintering temperature is lower than 200 °C, thermal decomposition did not occur and the body center cubic phase (bcc, JCPDS card no. 06–0175) of ZnCP remained (Supporting Information, Figure S5), although the TG measurement shows a little weight loss primarily due to the loss of water (Supporting Information, Figure S6). Interestingly, with the sintering temperature increased to 250 °C (Supporting Information, Figure S6), XRD pattern starts to exhibit the mixed phases of ZnCP and ZnO (Supporting Information, Figure S5b). As schematically shown in **Figure 3**, this

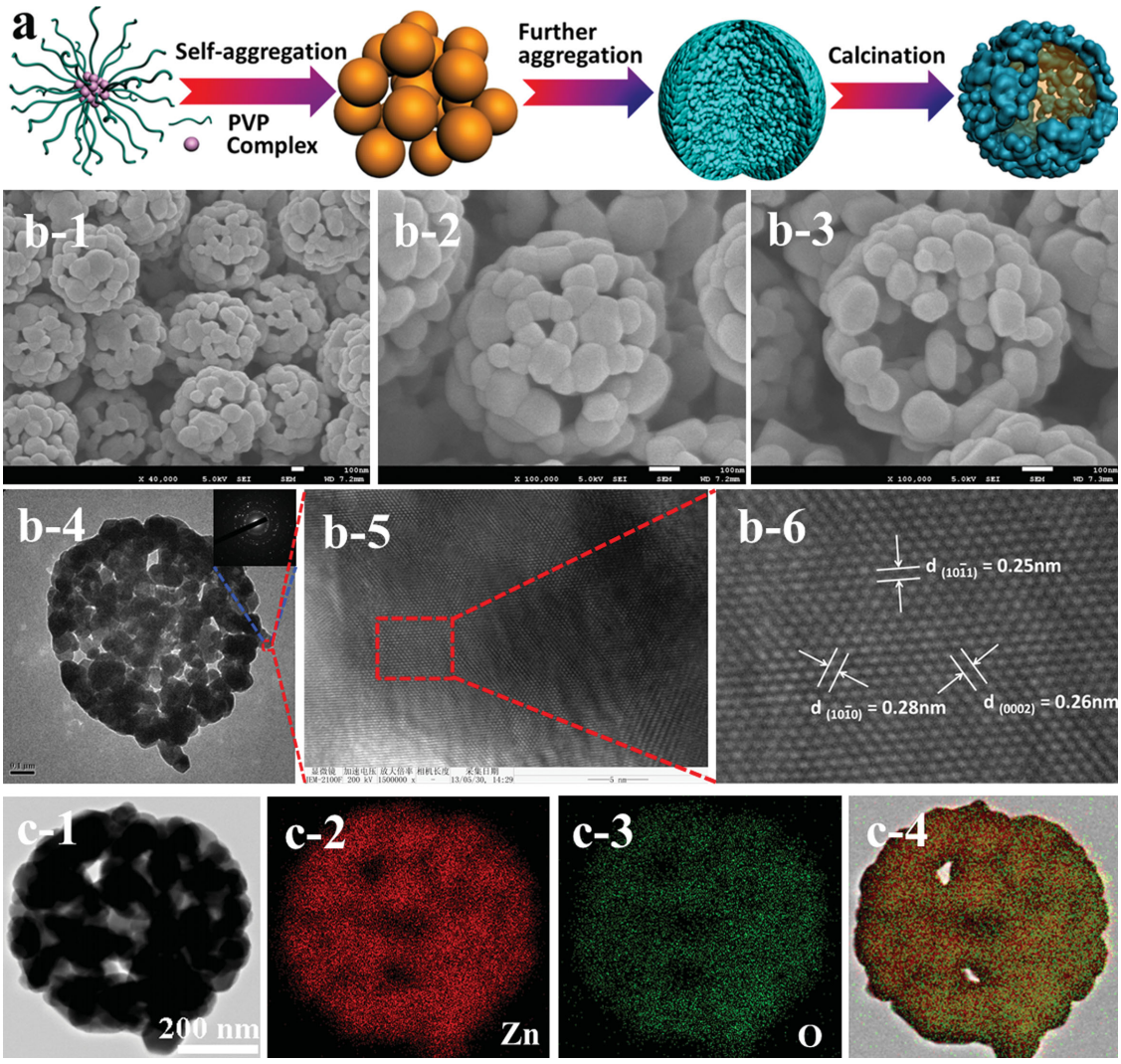

Figure 2. a) The formation mechanism of ZnO nanocages with a porous structure at 700 °C. b1–b6) SEM and TEM images of the obtained ZnO nanocages (inset in b-4) shows corresponding SAED pattern). c) HAADF-STEM and elemental mapping of a single ZnO nanocage. Scale bars for all the SEM images are 100 nm.

process could include two processes: the transformation from a single ZnCP nanocrystal to ZnO multinanocrytals and the transformation from the ZnCP microsphere to ZnO nanocage, respectively.

In the first process, the ZnCP nanocrystals on the surface of the microsphere begin to react and a core/shell-structured intermediate of ZnCP@ZnO is formed simultaneously (Figure 3A-a). Figure 3B-a,B-b shows that that hollow ZnO nanoparticles are formed around the out-shell of the ZnCP nanocrystal with TEM image around 250–300 °C. At the low temperature (around 250–300 °C) before the ZnCP thermal decomposition (no significant weight loss, as shown in Supporting Information, Figure S6),[27] the mechanism of the nanohollow ZnO prepared from the ZnCP nanocrystals should belong to a type of nanoscale Kirkendall based-process coupled with interfacial oxidation chemical reactions in air by the Cabrera and Mott effect.[28] Cabrera and Mott's lower-temperature oxidation effect occurs initially on the oxide surface on which oxygen atoms are adsorbed, and electrons can pass rapidly through the oxide by tunnelling to establish an equilibrium between the nanoZnCP's surfaces and adsorbed oxygen to create an electronic field in the thin oxide layer, which can pull metal ions through the oxide film (shown in Figure 3A-a,A-b), in which J_{ZnCP}, J_{O2}, and J_{void} are diffuse fluxes of atoms or ions from ZnCP, O_2 and void, respectively. Then, small Kirkendall voids will be generated when ZnCP in the inside-shell nanoparticles migrate across the ZnO surface layer and then contribute to the formation of a new ZnO layer. The second stage is dominated by Zn atomic or ionic (J_{ZnCP}) surface diffusion from the nanoZnCP core material along the pore surface to the reaction front as the dominant material transport process because of the much lower activation energy of surface diffusion than bulk diffusion. After all Zn atoms or ions (J_{ZnCP}) are consumed to react with oxygen ion from J_{O2} absorbed on the ZnO surface, nanohollow ZnO can be formed as a result of the vacancy clustering in the core as shown in Figure 3B-c. It can be expected that the

Part. Part. Syst. Charact. **2015**,
DOI: 10.1002/ppsc.201500011

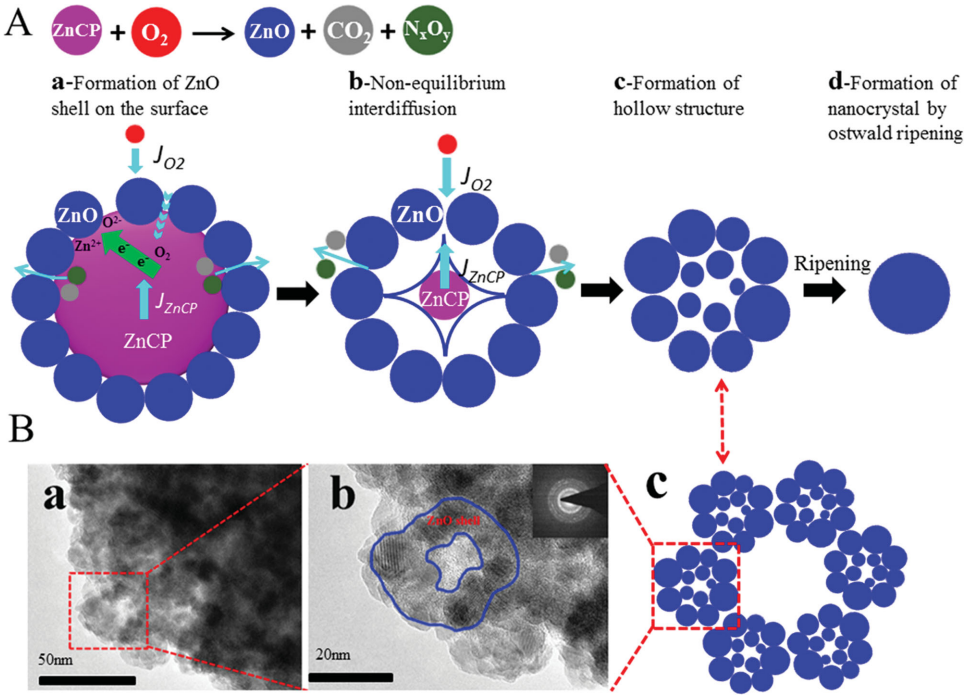

Figure 3. Schematic illustration of the preparation of ZnO nanocage: A) Transformation of a single ZnCP nanocrystal to ZnO nanocrystal based on nanoscale Kirkendall effect and Ostwald ripening (from 200 to 300 °C). B) TEM images of the as-prepared hollow structure of ZnO nanocrystal on the surface of a ZnCP sphere by calcination at 250 °C. Inset in (b) shows corresponding SAED pattern.

novel "hierarchical ZnO nanocages (about 500 nm diameters) embedded with smaller nanocages (about 25 nm diameters) with 10 nm nanocrystal" would be generated finally by this low temperature nanoscale Kirkendall effect.

The hollow structured ZnO grows into a single ZnO nanocrystal by Ostwald ripening (Figure 3A-d) around the temperature zone-2 (300–700 °C). When the sintering temperature is above 300 °C, ZnCP nanocystals fully change into ZnO nanocystals, which were all good consistent with the standard values for pure-phase ZnO with hexagonal close-packed structure (Supporting Information, Figure S5, hcp, JCPDS card no. 36–1451). The small ZnO nanoparticles will grow up by Ostwald ripening, which was the coarsening and recrystallization process of ZnO nanocrystals at higher temperature due to smaller nanocrystals possess higher interfacial energy compared with larger nanocrystals. The average sizes of ZnO nanocrystals are 19 nm at 300 °C, 32 nm at 400 °C, 46 nm at 500 °C, 77 nm at 600 °C, and 95 nm at 700 °C, respectively, measured from XRD data shown in Supporting Information, Table S1, exhibiting a size growth process as increasing annealing temperature. ZnO particles with different sizes and morphologies obtained from four calcination temperatures of 400, 500, 600, 700, and 800 °C are showed in Figure 2 and Supporting Information, Figure S8. At a relatively low temperature of 400 °C, the resulting ZnO particles retained the good spherical shape of original ZnCP microspheres (Supporting Information, Figure S7a). Magnified SEM image (Supporting Information, Figure S7b) reveals the ZnO particle was composed of aggregated nanocrystals with size of dozens of nanometers. Broken particles further demonstrate nanosphere was formed by the accumulation of nanocrystals (Supporting Information, Figure S7c). In this stage, ZnO particles had a diameter of about 750 nm, which is larger than that of the ZnO nanocages generated around 250 °C (500 nm), but smaller than that of ZnCP microspheres (1 μm). TEM image displays a relative dense inside of the ZnO particle (Supporting Information, Figure S7d). When the calcination temperature increased to 500 °C, voids started to appear due to the nanocrystals growth by coalescence of the adjacent small nanocrystals, as shown in the SEM image of a cracked nanosphere (Supporting Information, Figure S7g). TEM characterization obviously exhibits a relatively loose accumulation of nanocrystals (Supporting Information, Figure S7h). After calcination at an elevated temperature of 600 °C, ZnO nanocrystals continued to grow with the size reaching one hundred nanometers (Supporting Information, Figure S7i,j). Interestingly, ZnO hollow structure began to show facets of nanoZnO crystals during Ostwald ripening process, while the resultant ZnO nanocages still remained intact without any breakage, exhibiting the excellent structural stability.

When the sintering temperature finally increased to zone-3 (800 °C), which is higher than the temperature of ZnCP total decomposition according to TG shown in Supporting Information, Figure S6, the hollow ZnO structures are formed with porous shell through coalescence of the vacancies. This process is based on nanoscale Kirkendall effect through solid–gas interfacial reactions at higher temperature above decomposing precursor (ZnCP), which involves the nonequilibrium interdiffusion at gas state with volume loss to release of internally produced carbon dioxide (CO_2) and nitric oxide (N_xO_y) during the process of thermal decomposition. The conversion of ZnCP core to ZnO shell will be hindered by the as-formed ZnO layer as well as the inner diffusion of oxygen, further reaction will

continue by the diffusion of atoms or ions through the interface. It can be expected that the diffusion rate of Zn ions from the inner ZnCP during thermal decomposition is faster than that of atmospheric oxygen from outsides during the oxidation reactions, hence the preferred outward diffusion of Zn atoms or ions from ZnCP core to shell leads to a net material flux across the interface. Kirkendall voids are produced near the ZnO/ZnCP interface via interdiffusion due to the difference between diffuse fluxes ($J_{ZnCP} > J_{O2}$) by vacancy assisted exchange of material. The voids expand inward for subsequent inner flux of vacancies ($J_{void} = J_{ZnCP} - J_{O2}$).[29] Meanwhile, voids grow and coalesce into bigger ones due to a flow of fast-moving vacancies to the vicinity of the solid–gas interface, which establish new bridges as fast transport paths for the remaining ZnCP and eventually results in a hollow cavity. Hence, ZnO nanocages with a large cavity can be successfully prepared with bigger nanocrystal particles as the shell (Supporting Information, Figure S7m–p).

Furthermore, because the electronic properties are highly correlated to the defects in ZnO, here we measured the typical room temperature photoluminescence (PL) spectra of ZnO obtained at different temperatures and show them in **Figure 4**a. As we can see, all the samples show a typical luminescence behavior with the emission of a UV peak in the visible spectra region of ≈470 to 720 nm, which is commonly attributed to the deep level emission from ZnO due to the presence of point defects. To be specific, the PL transitions in the green region centered at ≈540 nm is due to the oxygen vacancies (V_O), and in the red orange region centered at ≈605 nm could be due to the oxygen interstitials (O_i).[30] Oxygen vacancies and interstitials are the key point defects and play a major role in determining the crystalline and compositional purity of ZnO.[31] It also can be observed that intensities of the UV peaks for V_O and O_i change with the calcination temperatures, and we can divide it into four regions: (II) as the temperature increases from 300 to 500 °C, the intensities of the UV peaks for V_O and O_i change slightly (the intensity of the UV peak of V_O first decreases and then increases, and the intensity of the UV peak of O_i increases all the time); (II) both the intensities of the UV peaks for V_O and O_i rise sharply when the temperature increases from 500 to 600 °C; (III) then they both come to a saturate state within the temperature range of 600 to 700 °C;(IV) finally, they both increase dramatically when the temperature increases to 800 °C. The increase in intensities of the UV peaks for V_O and O_i is due to the enhancement in the density of V_O and O_i.[32] Another phenomenon we should notice is that the intensity of the UV peak of V_O is lower than that of the UV peak of O_i when the temperature is 400—700 °C but get higher than that of the UV peak of O_i with two conditions, such as when the temperatures are at 300 °C and at 800 °C, which are related to Kirkendall process due to the lower temperature oxidation and higher temperature solid-gas interfacial reactions, respectively.

The density of the point defects is closely associated with their mobilities, and a diffusivity study of the point defects may help us to gain insights into the defect chemistry in general. Using density functional theory (DFT) calculations in conjunction with the climbing-image nudged elastic band (cNEB) method, Erhart et al. did a systematical study of the diffusion properties of oxygen vacancies, oxygen interstitials, zinc vacancies (V_{Zn}), and zinc interstitials (Zn_i),[9] and **Table 1** shows a summary of their results for the lowest energy barriers of different point defects diffusion. From Table 1, we can see that the energy barriers for oxygen vacancies and oxygen interstitials are higher than those for zinc vacancies and zinc interstitials under all the charge states, indicating a difficult migration for oxygen vacancies and oxygen interstitials and leading to the main V_O and O_i defects in ZnO.

For the PL spectra shown in Figure 4a, in the interval (I), the intensities of the UV peaks for V_O and O_i increase slightly with the temperature from 300 to 500 °C on the whole, which may be attributed to that the increasing temperature enhances the slow thermal decomposition of ZnCP and creates more amounts of Zn metals, thus creating more V_O and O_i in ZnO due to the fast diffusion of zinc interstitials in the bulk ZnO and Zn atoms on the ZnO boundaries. In the interval (III), the imbalance between the diffusion of V_O/O_i and V_{Zn}/Zn_i becomes smaller with the increasing temperature, thus compensating the increasing amount of point defects induced by the increasing temperature and leading to a saturate state for the density of V_O and O_i. For the intervals (II) (partial decomposition) and (IV) (total decomposition), the ZnCP structure may undergo a phase transformation with the stages of fast

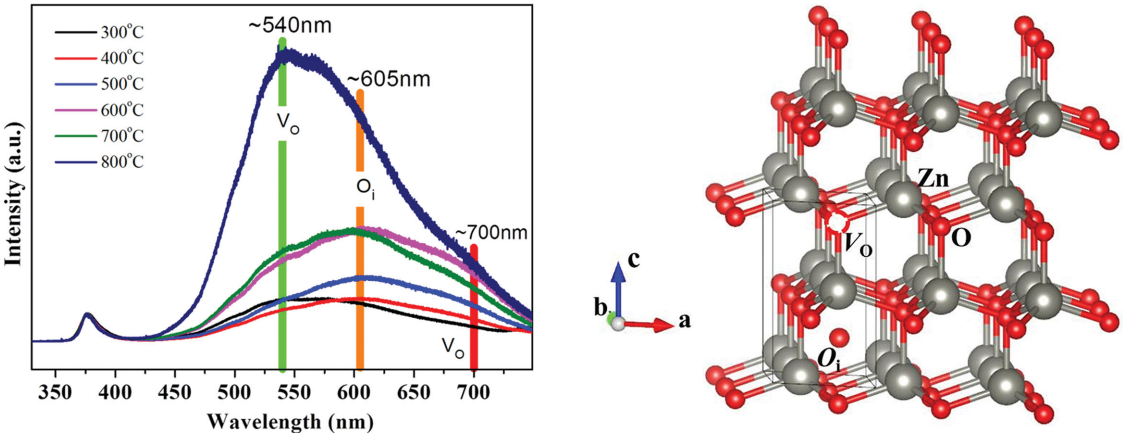

Figure 4. Room temperature PL spectra of ZnO obtained from different calcination temperatures. Spatial structure of ZnO with oxygen vacancies (V_O) and oxygen interstitials (O_i).

Part. Part. Syst. Charact. **2015**,
DOI: 10.1002/ppsc.201500011

Table 1. The lowest energy barriers of different point defects diffusion in ZnO in units of eV summarized from the systematical study by Erhart et al.[9]

Point defect	Charge state				
	$q=+2$	$q=+1$	$q=0$	$q=-1$	$q=-2$
V_O	1.09	1.37	1.87		
O_i	1.03	0.98	0.81	0.23	0.40
V_{Zn}			1.19	1.12	0.77
Zn_i	0.22	0.27	0.25		

decomposition of ZnCP according to the TG data as shown in Supporting Information, Figure S6. Note that at 800 °C (intervals (IV)), it can be expected that with the total decomposition of ZnCP, the faster diffusion of Zn atoms or ions from ZnCP at the gas state than that of oxygen atoms or ions from O_2 by nanoscale Kirkendall effect through solid–gas interfacial reactions could induce large amounts of V_O, thus leading to the dramatic increase in the intensities of the UV peaks for V_O due to their slow migration.

3. Conclusion

In summary, a facile and bottom–up approach has been demonstrated to prepare ZnO nanocages with porous shell structures, which was produced by thermally induced oxidative decomposition of a cyanide-bridged hybrid coordination polymer of ZnCP microspheres from 250 to 800 °C. The transformation of ZnCP microspheres to ZnO nanocages process was based on two types of nanoscale Kirkendall effect, which are related to lower temperature solid–solid interfacial oxidation and higher temperature solid–gas interfacial reaction, respectively. At the low temperature (around 300 °C) and before the ZnCP decomposition, the novel "hierarchical ZnO bigger nanocages embedded with smaller nanocages with 10 nm nanocrystals" can be generated. In contrast, when coming to the total decomposition of ZnCP at 800 °C, ZnO nanocages with significantly increased sizes and large cavities are generated, and large amounts of V_O are created at the same time, leading to the dramatic increased luminescence intensities of the UV peak due to V_O at 540 nm. Thus, the defect concentration in the prepared ZnO nanocages can be controlled by tuning the sintering temperatures. Such defect engineering is of crucial importance for its applications in electronics and optoelectronics.

4. Experimental Section

Synthesis of Monodispersed $Zn[Zn(CN)_4]\cdot xH_2O$ Microspheres (ZnCP): ZnCP microspheres were synthesized by a single-step aqueous solution co-precipitation method. In a typical procedure, 0.136 g $ZnCl_2\cdot 6H_2O$ (1 mmol) and 2.25 g PVP were dissolved into 100 mL ultrapure water to form a clear solution. Meanwhile, 1 mmol $K_2[Zn(CN)_4]$ was added into 100 mL ultrapure water to obtain another clear solution. Then the $K_2[Zn(CN)_4]$ solution was added into above solution drop by drop. After that, the mixed solution was stirred for 30 min and aged at room temperature for 24 h. The resultant white precipitation was collected by centrifugation and washed using ethanol and pure water several times and finally dried at 60 °C in a vacuum drying oven for subsequent characterization.

Conversion from ZnCP Microspheres into ZnO Nanocages: The crystallographic structures of the samples were characterized with X-ray diffraction in a typical conversion procedure, 50 mg ZnCP microspheres in a corundum crucible were calcinated at 700 °C for 6 h with a heating rate of 2 °C min^{-1} in air. In order to investigate the influence of sintering temperature on the crystal growth of ZnO nanocrystals, the microspheres were calcinated at several different temperatures from 200 to 800 °C following the same procedure.

Structure and Morphology Characterization: Morphology of all the products was characterized by scanning electron microscope (SEM, Hitachi S4700) and transmission electron microscope (TEM, JEOL JEM-2100F). X-ray diffraction (XRD) experiment was carried out on a Micscience M-18XHF (with CuKa radiation) instrument. PI of the ZnCP suspension was characterized using a Zetasizer (NanoZS) from Malvern Instruments.

Supporting Information

Supporting Information is available from the Wiley Online Library or from the author.

Acknowledgements

This work was substantially supported by MOST (2013AA031802) and Shenzhen Science and Technology Research Grant (Grant Nos. ZDSY20130331145131323, CXZZ20120829172325895, and JCYJ20120614150338154).

Received: January 29, 2015
Revised: February 15, 2015
Published online:

[1] C. Schilling, R. Theissmann, C. Notthoff, M. Winterer, *Part. Part. Syst. Charact.* **2013**, *30*, 434.
[2] D. Q. He, X. Sheng, J. Yang, L. P. Chen, K. Zhu, X. J. Feng, *J. Am. Chem. Soc.* **2014**, *136*, 16772.
[3] W. Xitao, L. Rong, W. Kang, *J. Mater. Chem. A* **2014**, *2*, 8304.
[4] a) R. Yu, C. Pan, J. Chen, G. Zhu, Z. L. Wang, *Adv. Funct. Mater.* **2013**, *23*, 5868; b) S. Niu, Y. Hu, X. Wen, Y. Zhou, F. Zhang, L. Lin, S. Wang, Z. L. Wang, *Adv. Mater.* **2013**, *25*, 3701.
[5] Z.-Y. Zhang, Y.-D. Xu, Y.-Y. Ma, L.-L. Qiu, Y. Wang, J.-L. Kong, H.-M. Xiong, *Angew. Chem. Int. Ed.* **2013**, *52*, 4127.
[6] a) Q. Zhang, T. P. Chou, B. Russo, S. A. Jenekhe, G. Cao, *Angew. Chem. Int. Ed.* **2008**, *47*, 2402; b) X. Wang, Z. Chen, D. Liu, W. Tian, Q. Wang, C. Zhang, J. Liu, L. Han, Y. Bando, D. Golberg, *Part. Part. Syst. Charact.* **2014**, *31*, 757.
[7] L. Vayssieres, K. Keis, S.-E. Lindquist, A. Hagfeldt, *J. Phys. Chem. B* **2001**, *105*, 3350.
[8] Z. Dong, X. Lai, J. E. Halpert, N. Yang, L. Yi, J. Zhai, D. Wang, Z. Tang, L. Jiang, *Adv. Mater.* **2012**, *24*, 1046.
[9] a) P. Erhart, K. Albe, *Appl. Phys. Lett.* **2006**, *88*, 201918; b) P. Erhart, K. Albe, *Phys. Rev. B* **2006**, *73*, 115207.
[10] a) G. Moussa, U. B. Demirci, S. Malo, S. Bernard, P. Miele, *J. Mater. Chem. A* **2014**, *2*, 7717; b) W. Shi, X. Zhang, G. Che, *Int. J. Hydrogen Energy* **2013**, *38*, 7037.
[11] a) C. Yuan, J. Li, L. Hou, L. Zhang, X. Zhang, *Part. Part. Syst. Charact.* **2014**, *31*, 657; b) H. Wan, J. Jiang, Y. Ruan, J. Yu, L. Zhang, H. Chen, L. Miao, S. Bie, *Part. Part. Syst. Charact.* **2014**, *31*, 857.
[12] Y. Piao, J. Kim, H. B. Na, D. Kim, J. S. Baek, M. K. Ko, J. H. Lee, M. Shokouhimehr, T. Hyeon, *Nat. Mater.* **2008**, *7*, 242.

[13] a) F. Caruso, R. A. Caruso, H. Möhwald, *Science* **1998**, *282*, 1111; b) X. W. Lou, C. M. Li, L. A. Archer, *Adv. Mater.* **2009**, *21*, 2536; c) J. Yang, T. Sasaki, *Chem. Mater.* **2008**, *20*, 2049; d) Q. Peng, Y. Dong, Y. Li, *Angew. Chem. Int. Ed.* **2003**, *42*, 3027.

[14] a) Y. Yin, R. M. Rioux, C. K. Erdonmez, S. Hughes, G. A. Somorjai, A. P. Alivisatos, *Science* **2004**, *304*, 711; b) H. J. Fan, U. Gösele, M. Zacharias, *Small* **2007**, *3*, 1660; c) Y. Jiang, S. Zhang, Q. Ji, J. Zhang, Z. Zhang, Z. Wang, *J. Mater. Chem. A* **2014**, *2*, 4574.

[15] a) J. G. Yu, H. Guo, S. A. Davis, S. Mann, *Adv. Funct. Mater.* **2006**, *16*, 2035; b) H. G. Yang, H. C. Zeng, *J. Phys. Chem. B* **2004**, *108*, 3492; c) C. C. Yec, H. C. Zeng, *J. Mater. Chem. A* **2014**, *2*, 4843.

[16] X. W. Lou, C. Yuan, Q. Zhang, L. A. Archer, *Angew. Chem. Int. Ed.* **2006**, *45*, 3825.

[17] Y. Xiong, B. Wiley, J. Chen, Z.-Y. Li, Y. Yin, Y. Xia, *Angew. Chem. Int. Ed.* **2005**, *44*, 7913.

[18] a) S.-H. Lo, C.-H. Chien, Y.-L. Lai, C.-C. Yang, J. J. Lee, D. S. Raja, C.-H. Lin, *J. Mater. Chem. A* **2013**, *1*, 324; b) H. R. Moon, D.-W. Lim, M. P. Suh, *Chem. Soc. Rev.* **2013**, *42*, 1807; c) L. J. Murray, M. Dinca, J. R. Long, *Chem. Soc. Rev.* **2009**, *38*, 1294; d) W. Xuan, C. Zhu, Y. Liu, Y. Cui, *Chem. Soc. Rev.* **2012**, *41*, 1677.

[19] a) Z. Guo, H. Wu, G. Srinivas, Y. Zhou, S. Xiang, Z. Chen, Y. Yang, W. Zhou, M. O'Keeffe, B. Chen, *Angew. Chem. Int. Ed.* **2011**, *50*, 3178; b) S. Xiang, W. Zhou, Z. Zhang, M. A. Green, Y. Liu, B. Chen, *Angew. Chem. Int. Ed.* **2010**, *49*, 4615.

[20] L. Zhang, H. B. Wu, S. Madhavi, H. H. Hng, X. W. Lou, *J. Amer. Chem. Soc.* **2012**, *134*, 17388.

[21] M. Hu, S. Furukawa, R. Ohtani, H. Sukegawa, Y. Nemoto, J. Reboul, S. Kitagawa, Y. Yamauchi, *Angew. Chem. Int. Ed.* **2012**, *51*, 984.

[22] N. Yan, L. Hu, Y. Li, Y. Wang, H. Zhong, X. Hu, X. Kong, Q. Chen, *J. Phys. Chem. C* **2012**, *116*, 7227.

[23] M. Hu, A. A. Belik, M. Imura, Y. Yamauchi, *J. Am. Chem. Soc.* **2012**, *135*, 384.

[24] a) W. Lin, W. J. Rieter, K. M. L. Taylor, *Angew. Chem. Int. Ed.* **2009**, *48*, 650; b) T. Tsuruoka, S. Furukawa, Y. Takashima, K. Yoshida, S. Isoda, S. Kitagawa, *Angew. Chem. Int. Ed.* **2009**, *48*, 4739; c) J. Puigmartí-Luis, M. Rubio-Martínez, U. Hartfelder, I. Imaz, D. Maspoch, P. S. Dittrich, *J. Am. Chem. Soc.* **2011**, *133*, 4216.

[25] a) S. H. Lapidus, G. J. Halder, P. J. Chupas, K. W. Chapman, *J. Am. Chem. Soc.* **2013**, *135*, 7621; b) I. E. Collings, A. B. Cairns, A. L. Thompson, J. E. Parker, C. C. Tang, M. G. Tucker, J. Catafesta, C. Levelut, J. Haines, V. Dmitriev, P. Pattison, A. L. Goodwin, *J. Am. Chem. Soc.* **2013**, *135*, 7610.

[26] a) J. Wu, F. Duan, Y. Zheng, Y. Xie, *J. Phys. Chem. C* **2007**, *111*, 12866; b) L. Li, Y. Cheah, Y. Ko, P. Teh, G. Wee, C. Wong, S. Peng, M. Srinivasan, *J. Mater. Chem. A* **2013**, *1*, 10935.

[27] a) M.-H. Park, Y. Cho, K. Kim, J. Kim, M. Liu, J. Cho, *Angew. Chem. Int. Ed.* **2011**, *50*, 9647; b) J. Liu, D. Xue, *Adv. Mater.* **2008**, *20*, 2622; c) X. Xia, Y. Wang, A. Ruditskiy, Y. Xia, *Adv. Mater.* **2013**, *25*, 6313.

[28] N. Cabrera, *Philos. Mag.* **1949**, *40*, 175.

[29] a) W. Wang, M. Dahl, Y. Yin, *Chem. Mater.* **2013**, *25*, 1179; b) H. J. Fan, M. Knez, R. Scholz, D. Hesse, K. Nielsch, M. Zacharias, U. Gösele, *Nano Lett.* **2007**, *7*, 993.

[30] a) X. M. Fan, J. S. Lian, Z. X. Guo, H. J. Lu, *Appl. Surf. Sci.* **2005**, *239*, 176; b) H. B. Zeng, Z. G. Li, W. P. Cai, P. S. Liu, *J. Appl. Phys.* **2007**, *102*, 104307; c) C. H. Ahn, Y. Y. Kim, D. C. Kim, S. K. Mohanta, H. K. Cho, *J. Appl. Phys.* **2009**, *105*, 013502; d) N. H. Alvi, K. U. Hasan, O. Nur, M. Willander, *Nanoscale Res. Lett.* **2011**, *6*, 130.

[31] a) A. F. Kohan, G. Ceder, D. Morgan, C. G. Van de Walle, *Phys. Rev. B* **2000**, *61*, 15019; b) A. Janotti, C. G. Van de Walle, *Phys. Rev. B* **2007**, *76*, 165202.

[32] L. M. Kukreja, P. Misra, J. Fallert, D. M. Phase, H. Kalt, *J. Appl. Phys.* **2012**, *112*,013525.

Part. Part. Syst. Charact. **2015**,
DOI: 10.1002/ppsc.201500011